Journal of Materials Research and Technology 27 (2023) 3170–3179

Contents lists available at ScienceDirect

Journal of Materials Research and Technology

journal homepage: www.elsevier.com/locate/jmrt

Emissivity measurements conducted on intermetallic γ-TiAl-based alloys for aeronautical applications

L. Usategui [a], I. López-Ferreño [a,*], T. Echániz [b], M. Sainz-Menchón [c], M. Musi [d], H. Clemens [d], G.A. López [c]

[a] Applied Mathematics, University of the Basque Country (UPV/EHU), E-01006 Vitoria-Gasteiz, Spain
[b] Applied Mathematics, University of the Basque Country (UPV/EHU), E-48013 Bilbao, Spain
[c] Physics Department, University of the Basque Country (UPV/EHU), E-48940 Leioa, Spain
[d] Department of Materials Science, Montanuniversität Leoben, Franz Josef-Str. 18, 8700 Leoben, Austria

ARTICLE INFO

Keywords:
A. Intermetallics
B. Surface properties
Thermal properties and oxidation
D. Microstructure
F. Spectroscopic methods
Various and electron microscopy
Scanning
G. Aero-engine components

ABSTRACT

The directional spectral emissivity of a Ti–48Al–2Nb–2Cr alloy (in at.%), 4822 alloy, and a Ti-43.5Al–4Nb–1Mo-0.1B alloy (in at.%),TNM alloy, used in the aeronautical industry, are measured between 150 and 850 °C. The differences in the emissivity values between both alloys at the lowest temperatures, indicates that the β_o phase, only present in TNM, exhibit higher emissivity values. By numerical integration of the measured data, the total directional and hemispherical emissivity have been calculated. At 850 °C the total hemispherical emissivity in vacuum are nearly identical with 0.274 ± 0.006 for the 4822 alloy and 0.273 ± 0.007 for the TNM alloy. The lower emissivity change with temperature measured in TNM alloys is related with the deconvolution of β_o phase by diffusion processes. Afterwards, near-normal spectral emissivity measurements are performed in both alloys during isothermal oxidation treatments at 750 °C and 850 °C for 120 h. The emissivity data reveal that the TNM alloy exhibits higher oxidation resistance especially at 750 °C. In parallel, microstructural characterization has been performed before the measurements, after the directional emissivity measurements prior to oxidation and after isothermal oxidations. The formed oxide scale is composed of four layers that coincide with those reported in the literature: an outer layer of TiO_2 contiguous with a layer of Al_2O_3, followed by a TiO_2/Al_2O_3 mixed layer and finally a thin layer of Nb-rich nitride. This mixed layer governs the interferential part of the alloys' emissivity spectra, which, in combination with the background, determines the overall radiative behavior of the alloys under service conditions.

1. Introduction

Aeronautical Ni-base superalloys currently dominate the field of turbine blades in jet engines, due to their ability to withstand highly demanding mechanical and thermal loads. Their development began in the 1940's [1] and they are still used in the hottest part of the engine, where temperatures can exceed 1000 °C, due to their exceptional mechanical resistance at high temperatures, resistance to creep and resistance to corrosion [1,2]. However, the importance of improving the environmental compatibility, safety and the economic performance of transport systems has triggered the replacement of heavy Ni alloys (>8 g/cm^3) by lightweight intermetallic γ-TiAl-based alloys with only half the specific weight (3.9–4.2 g/cm^3) and interesting high-temperature properties up to 750 °C [3–5]. Among the different γ-TiAl alloys two main compositions were successfully developed and implemented in the aeronautical sector. The 4822 alloy (Ti–48Al–2Nb–2Cr (in at.%)), which is already present in the low-pressure turbines of General Electric's GEnX engine since 2011, and the TNM alloy (Ti-43.5Al–4Nb–1Mo-0.1B (in at.%)), which was developed more recently and introduced in Pratt & Whitney's Geared Turbofan engine in 2014 [3,6]. The 4822 alloy solidifies peripatetically and mainly consists of the two phases γ-TiAl and α_2-Ti_3Al with a small amount of ordered β_o-TiAl phase [7], whereas the TNM alloy solidifies completely via the disordered β phase and is composed of three phases $\gamma + \alpha_2 + \beta_o$ at room temperature [5]. All three phases, tetragonal γ-TiAl, hexagonal α_2-Ti_3Al and body-centered cubic β_o-TiAl are atomically ordered phases, showing $L1_0$, $D0_{19}$ and B2 crystal structures, respectively. In the case of the β_o phase, the ordering occurs at 1175–1205 °C temperature range [8], while at higher temperatures

* Corresponding author.
E-mail address: inaki.lopez@ehu.eus (I. López-Ferreño).

https://doi.org/10.1016/j.jmrt.2023.10.163
Received 11 September 2023; Accepted 16 October 2023
Available online 19 October 2023

this phase is stable in its disordered form, i.e. β phase, thus, exhibiting better ductility and improving the hot-workability of the material. These two alloys have a limited service temperature of 700–750 °C, due to their insufficient oxidation resistance and their lack of creep strength at higher temperatures [3,7,9]. In order to increase their service temperature and high-temperature creep strength, as well as to achieve a more extensive industrial exploitation of these alloys, oxidation resistance at elevated temperature has to be improved. Therefore, significant efforts are being made to understand the microstructure and its evolution during oxidation processes, as well as its effect on mechanical properties [9–13]. Accordingly, the identification and quantification of heat transfer parameters, in order to characterize thermal loadings and heat loss of such alloys, are mandatory. To that end, the measurement of emissivity, which is defined as the ratio between the radiation emitted by a given body and the radiation of a blackbody at the same temperature [14], is crucial. The emissivity is a property that governs the heat exchange of a material with its surrounding at high temperature via thermal radiation. Specifically, infrared emissivity measurements at the service temperature of alloys are essential to assess, for example, their self-cooling capacity [15], with the high-emitting materials being the most capable of such feature. Furthermore, the emissivity is strongly dependent on microstructure, roughness of the surface, emission angle, as well as temperature. In this vein, emissivity measurements allow the observation of surface processes, such as oxidation [16–18], and events that occur on the entire material and which are reflected on the surface. The knowledge of this single parameter is very important in high-temperature environments such as airplane turbines, not only for determining the temperature distribution inside the turbine, but also for the evaluation of microstructural changes taking place in the blades during employment. Additionally, given the growing interest in additive manufacturing processes and their use for the synthesis of aeronautical alloys [19–21], it is necessary to characterize precisely the spectral emissivity to be able to remotely measure the temperature *in situ* during the process, and, thus, optimize the synthesis through an accurate temperature control [20]. Moreover, during such a processing, where materials experience a complex thermal history involving directional heat extraction during repeated melting and rapid solidification, emissivity is essential to simulate the temperature fields and gradients of the parts upon production.

According to the best knowledge of the authors, no research work containing the emissivity data for the 4822 alloy and the TNM alloy has been published. In this work, the emissivity properties of these two engineering γ-TiAl-based alloys use in aerospace applications are presented. Both directional and hemispherical emissivity dependences on the radiation wavelength (2–22 μm) and sample temperature (150–850 °C) have been studied under vacuum. Furthermore, isothermal oxidation processes in air at 750 °C and 850 °C of both alloys have been studied via normal emissivity measurement, amended by a complete microstructural characterization.

2. Material and methods

2.1. TiAl alloys

In the current study, two engineering γ-TiAl based alloys were employed. The 4822 alloy was manufactured via additive manufacturing by means of electron beam melting (EBM), whereas the TNM alloy was produced by means of ingot metallurgy via vacuum arc remelting and centrifugal casting in permanent molds as described in [22]. The actual compositions in atomic percentage are presented in Table 1. In each alloy, the total amount of interstitial elements (O + N) was below 1200 wt. ppm. The chemical composition was measured via X-ray fluorescence spectroscopy (XRF) for Ti, Al, Nb, Cr, and Mo, and carrier gas hot extraction (CGHE) for O and N. For B inductively coupled plasma-optical emission spectroscopy (ICP-OES) was used.

Table 1
Composition of the investigated 4822 and TNM alloy in at.%.

Alloy	Ti	Al	Nb	Cr	Mo	B
4822	bal.	48.13	1.89	2.02	–	–
TNM	bal.	42.83	4.05	–	1.02	0.11

2.2. Emissivity

The emissivity measurements of the samples were carried out by means of the highly accurate self-made emissometer of the University of the Basque Country (UPV/EHU), a device capable of measuring directional spectral emissivity values with high accuracy at high temperatures in vacuum under controlled atmosphere [23]. The emissometer consists of a Fourier-transform infrared spectrometer (FTIR), a vacuum sample chamber, a reference blackbody (Isotech Pegasus R®) and an optical entrance box that allows switching between the blackbody source and the sample chamber by rotating a plane mirror. A detailed description of the equipment and the measurement and calibration methods employed in this paper was previously published [23].

The samples remained under controlled atmosphere during the whole measurement and a resistance heater was used as the heat source. The temperature of the sample was measured by two K type thermocouples spot-welded onto the surface of the material, separated 10 mm from each other and away from the measuring spot that corresponds to a 3.5 mm diameter spot centered at the sample.

In the first set of emissivity measurements the samples remained under vacuum ($4{\cdot}10^{-4}$ mbar at room temperature (RT)) and a small zirconium sample (33 mm^2) was attached on top of each sample to play as oxygen getter inside the chamber to minimize potential oxidation. Under these conditions, directional spectral emissivity measurements were performed on both the 4822 and TNM alloy in the 150–850 °C temperature range every 100 °C, obtaining 8 directional measurements (between 10 and 80° every 10° from the normal direction) for each temperature. The total directional emissivity was calculated using the following equation:

$$\varepsilon_T(\theta,T)=\frac{\int_0^\infty \varepsilon(\lambda,\theta,\varphi,T)\,L_{bb}(\lambda,T)d\lambda}{\int_0^\infty L_{bb}(\lambda,T)d\lambda} \quad (1)$$

where θ is the polar angle, φ is the azimuthal angle, L_{bb} is the radiance of a blackbody as given by Planck's law, and ε_T stands for the total directional emissivity (total normal, in the special case of $\theta = 0$).

Total hemispherical emissivities ε_H were calculated by interpolating the total directional values between 0 and 90° and integrating for the entire solid angle:

$$\varepsilon_H(T)=\int_0^{\pi/2}\varepsilon_T(\theta,T)\sin 2\,\theta d\theta \quad (2)$$

The azimuthal angle φ is assumed to bear no influence [23]. In order to propagate the uncertainties of these quantities, a Monte Carlo random-number sampling procedure has been used, where the inputs in the integral calculations are modelled as probability distributions based on their statistical properties [24]. Furthermore, an extrapolation procedure to introduce unbiased estimations of the amount of radiation outside the measured spectral range was applied, based on the well-known spectrally monotonic emissivities of metals. The contribution of these off-range integrations in Eq. (1) remained a small part of the total weight for all temperatures under study [23].

In the second set of emissivity measurements samples from both alloys were isothermally oxidized in the emissometer under laboratory air at 750 and 850 °C for 120 h and the emissivity at 10° (near-normal emissivity) was continuously measured to observe its evolution.

2.3. Microstructural characterization

Microstructural characterization techniques were employed to understand the microscopic changes responsible for the evolution of the thermal radiative properties of these alloys. Scanning electron microscopy (SEM) was used to characterize both samples before and after the spectral emissivity measurements under vacuum and also after the *in situ* oxidation study in air performed in the emissometer. For this purpose, Jeol JSM 6400/7000F electron microscopes equipped with Oxford Instruments LINK ISIS EDX spectrometers were employed. Cross-sections of the samples were mechanically polished with diamond paste of particle size down to 1 μm and completed with colloidal silica suspension of 0.05-μm particle size. In the case of oxidized samples, on the one hand, the surface appearance was investigated and, on the other hand; cross-sections of the oxide scales were analyzed. For analyzing the cross-sections, the samples were encapsulated in epoxy resin and then mechanically polished using the mechanical polishing described above, after which a thin layer of carbon was deposited to guarantee the necessary electrical conductivity.

In the case of oxidized samples, an X-ray diffraction (XRD) study has been carried out to identify the different phases present in the oxide scale. For this objective, an XPert-Pro diffractometer using Cu K_α radiation in Bragg–Brentano geometry with an angular step size of 0.02° was employed. Complementary X-ray photoelectron spectroscopy (XPS) depth profiles measurements were performed in a SPECS SYSTEM equipped with a Phoibos 150 1D-DLD analyzer and a monochromatic Al K_α source. The thickness was determined using a Ta_2O_5 reference with Ar^+ sputtering. The ion energies applied were 3000 and 5000 eV, respectively.

3. Results and discussion

3.1. Initial microstructure

Before measuring the spectral emissivity a microstructural characterization was conducted for both alloys. As it can be seen in Fig. 1, both alloys present a duplex microstructure that consists in the initial condition primarily of α_2/γ lamellar colonies and single-phase γ, α_2 and β_o grains situated at the colony boundaries. The main difference between the alloys is the amount of β_o phase, which appears in negligible quantities in the 4822 alloy. In fact, this 4822 alloy is often considered as a two-phase $\gamma + \alpha_2$ alloy [7]. Contrarily, the TNM alloy contains approximately 15 % of β_o phase (as determined by image analysis of Fig. 1b), which can be found mainly between but also within the individual α_2/γ colonies.

In addition, the roughness of the polished samples was studied previous to the emissivity measurements using a Mitutoyo® SJ-201 surface roughness tester. These measurements are necessary to be able to compare emissivity data in a reliable way, as the emissivity varies with the roughness of the studied sample. The surface parameters are shown in Table 2, where R_a is the average roughness, R_q the root-mean-square roughness, R_z the average maximum height, and R_{Sm} stands for the mean spacing between profile elements. Both alloys present similar values, with the exception of the mean spacing, where the TNM sample presents a lower value.

3.2. Emissivity measurements under vacuum

Normal spectral emissivity data for the 4822 and TNM alloy are shown in Fig. 2. In both cases the low-temperature measurements are noisier at short wavelengths due to the lower signal/noise ratio at those wavelengths. The uncertainties of these measurements are not presented here due to accumulation of data in a small area. The 4822 alloy shows the typical metallic behavior, which presents a relatively low emissivity that monotonically decreases with wavelength and increases with temperature [14]. The TNM alloy, unlike the 4822 alloy, shows very little temperature dependence.

In addition, even though the samples were measured in high-vacuum, the stronger increase in emissivity at short wavelengths at 750 and 850 °C with respect to the rest of the curves suggests the possibility of a slight oxidation at high temperatures on the surface of both samples. The initial stage of an oxidation process in a metal translates into the increase of the emissivity at shorter wavelengths [16]. This potential issue in both samples will be addressed in the next section.

Fig. 3 depicts a normal spectral emissivity comparison between different aeronautical alloys in the 150–267 °C range. Among the alloys analyzed in this study, data from Ni-base alloys [25–28] and Ti–6Al–4V [29] are presented. Although there is data dispersion even between Ni- and Ti-base alloys, all alloys have the same qualitative behavior, i.e. the low emissivity values monotonically decrease with wavelength increase. Besides, both of the alloys studied in the current work, despite having distinct values, have almost the same dependence on the wavelength, a feature they do not share with other presented data. Analogously, both Inconel alloys share an almost exact behavior.

Angle-dependent measurements between 10 and 80° were performed at each temperature. Fig. 4 shows the directional emissivity for both alloys at the lowest and highest temperatures in the investigated range, where the shades show the estimated standard uncertainties. As can be clearly observed for both alloys, lower-temperature measurements have much higher uncertainties, mainly due to the lower acquired

Table 2
Roughness parameters of the sample surface (in μm).

Alloy	R_a	R_q	R_z	R_{Sm}
4822	0.07	0.09	0.58	948
TNM	0.09	0.12	0.74	318

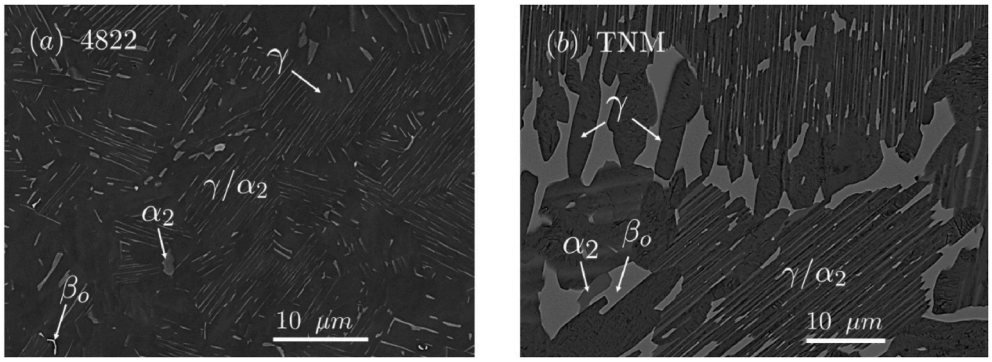

Fig. 1. Scanning electron microscope images taken in back-scattered electron (BSE) mode of the 4822 (a) and TNM (b) alloy obtained with an electron acceleration voltage of 10 kV.

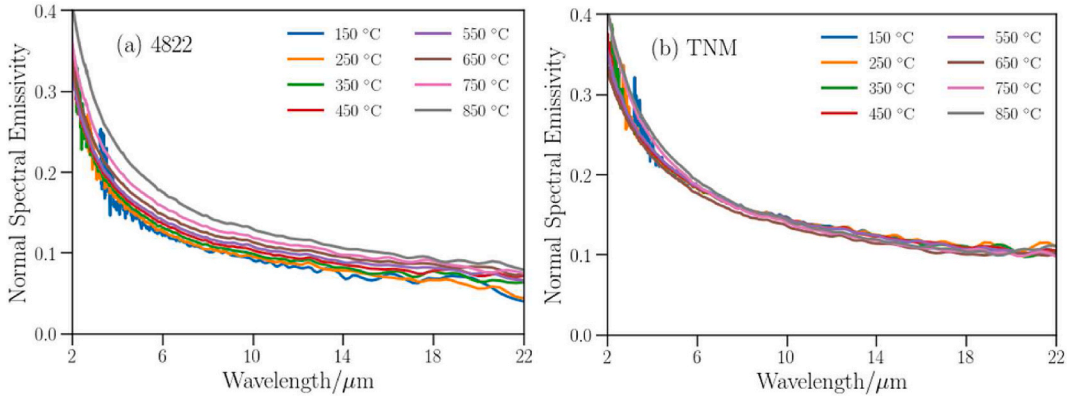

Fig. 2. Temperature-dependent normal spectral emissivity measurements for (a) 4822 and (b) TNM samples conducted between 150 and 850 °C.

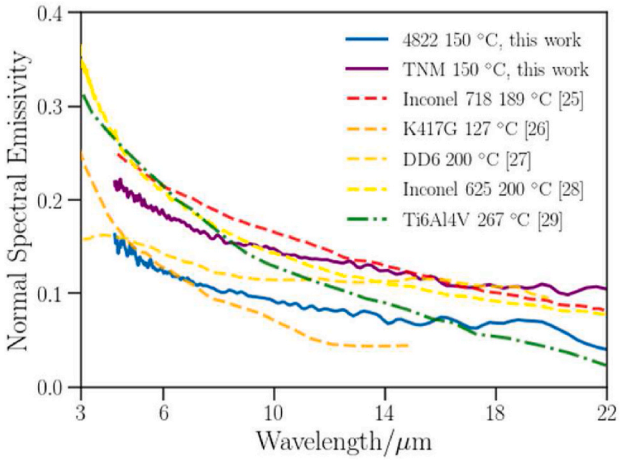

Fig. 3. Comparison between the temperature-dependent normal spectral emissivity measurements for the 4822 alloy and the TNM alloy at 150 °C (blue and orange curve, respectively) and various aeronautical alloys [25–29].

signal and the more significant influence of the low-temperature blackbody and surrounding temperatures (see details regarding the uncertainties budget in Ref. [23]). These directional measurements show the usual metallic behavior in both alloys [14]. The emissivity is almost constant from 10 to 40°, and then increases up until it reaches a maximum between 70 and 80°. The position of the maxima will depend on the complex refractive index and the relation between its real (n) and imaginary (k) parts. As the refractive index exhibits a different behavior at higher temperatures in the two alloys, different emissivity values are observed. Besides, at high temperatures and short wavelengths ($\lambda < 4$ μm), a different behavior is seen, especially for the TNM alloy. The emissivity, after staying constant for smaller angles, decreases at higher ones, a behavior often observed in ceramic materials that is consistent with the appearance of a thin semi-transparent oxide layer.

This metallic behavior evolution can also be seen in the total directional emissivities depicted in Fig. 5. Both samples show a metallic behavior at both depicted temperatures, with the emissivity showing the maximum value at high angles. Nevertheless, the 4822 total maximum value shifts from 80 to 70° from the lowest to the highest investigated temperature. Additionally, the emissivity increase between 40 and 80° in the TNM sample is clearly diminished. Values at 0° are considered to be equal to the 10° measurement and at 90° are equal to zero as the electromagnetic equations predict. The complete integration process is explained in detail in Ref. [23].

The calculated total hemispherical emissivity values are shown in Fig. 6. Both alloys present an increase with temperature, due to the combination of the increase of the spectral emissivity with temperature and the integral weight shift towards shorter wavelengths, where the emissivity values are higher. Once again, a slightly steeper increase at higher temperatures that can be attributed to a slight oxidation appearing from 650 °C onwards.

After measuring the directional emissivity under vacuum ($4 \cdot 10^{-4}$ mbar) at different temperatures up to 850 °C, the surface microstructure of both alloys has been studied, which is shown in Fig. 7. Both alloys formed a very thin oxide layer composed of sub-micrometer-sized oxide particles, which is consistent with the emissivity measurements. In the case of the 4822 alloy, the oxide particles are uniformly distributed throughout the surface (Fig. 7a). These oxide particles are needle-shaped or long rod with facets (Fig. 7a), where the maximum length is around 100 nm. In the case of the TNM alloy, the arrangement of the oxide particles is not uniform and two types of morphologies could be differentiated: there is a larger region with oxide particles similar to those found in the 4822 alloy, but of a slightly smaller size (Fig. 7b), and another regions composed of significantly smaller globular-shaped oxide particles (Fig. 7c). These characteristics indicate that the TNM sample has oxidized less than the 4822 one, which is consistent with the fact that the evolution of the total hemispherical emissivity and its corresponding directional emissivity as a function of temperature is lower in the TNM alloy.

XPS spectra were acquired at different depths of the thin oxide layers of both alloys to study the chemical composition and their thicknesses. In Fig. 8 spectra for Ti (a) and Al (b) spectra corresponding to the most superficial area of the oxide layer (initial state or surface) and to the area just below the oxide layer (final state or bulk) are presented. The outermost layers show significant peaks of oxidized Ti, particularly in the 4822 sample. Interestingly, these Ti peaks in the outermost layers are notably smaller than those observed in the bulk, suggesting a lower proportion of Ti in the oxide compared to the bulk (TiAl). These findings are in line with the presence of TiO_2 rutile particles at the surface. In addition, as depth increases both samples showed XPS signals corresponding to a mix of oxidized and metallic Ti and Al (not reproduced here). Subsequent sputtering led to reaching deeper areas, where only metallic Ti and Al were detected which depicts the bulk material and the end of the oxide layer. The thickness of the oxide scale of the 4822 and TNM samples have been estimated to be 226 nm and 147 nm, respectively. In the innermost sections of the 4822 sample scale, Nb was detected, whereas Nb and also Mo signals were found in the TNM sample. It was observed that these elements were not present in the most superficial layer of the scale. The oxide thicknesses obtained via XPS are in good agreement with the size of the oxide particles observed by microscopy (Fig. 7 a-b) and it is evident that in the case of 4822 the oxide layer is larger than in TNM. In any case, it worth mentioning that the areas analyzed during the XPS-depth profiling, used for the thickness determination, are significantly larger than those investigated by SEM and these results should only be considered qualitatively consistent.

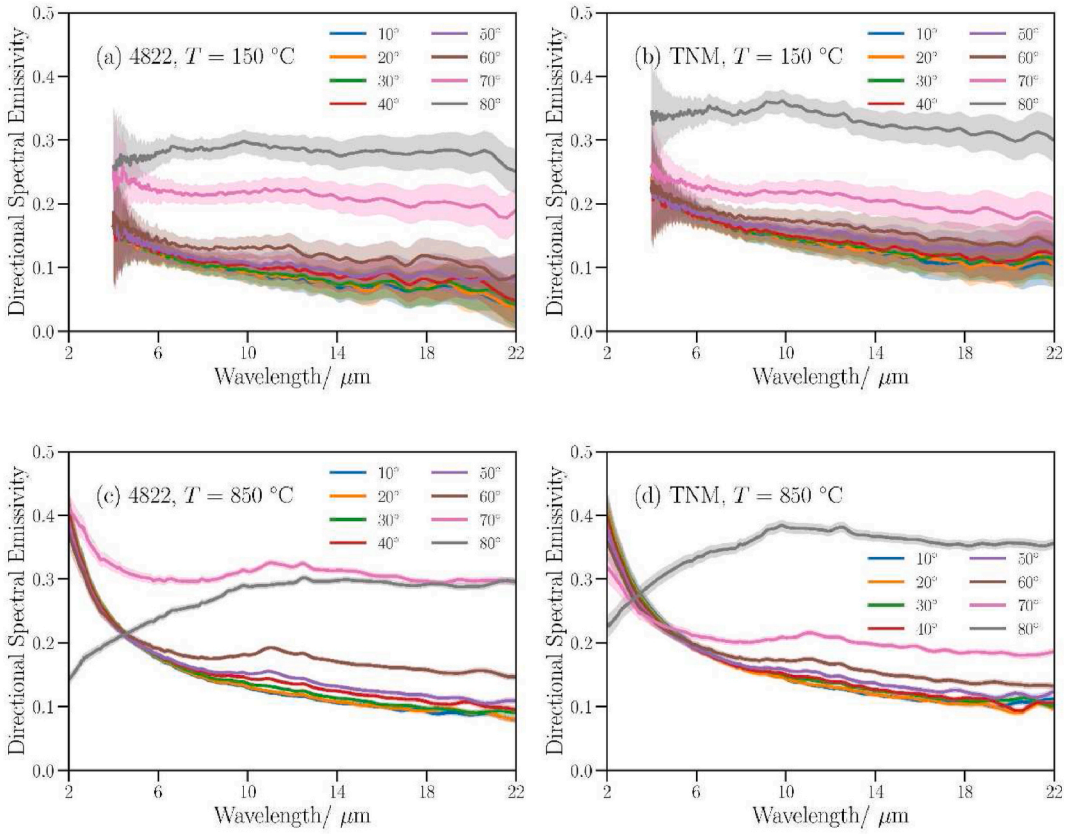

Fig. 4. Angular-dependent normal spectral emissivity measurements at 150 °C for (a) 4822 alloy and (b) TNM alloy and at 850 °C for (c) 4822 alloy and (d) TNM alloy.

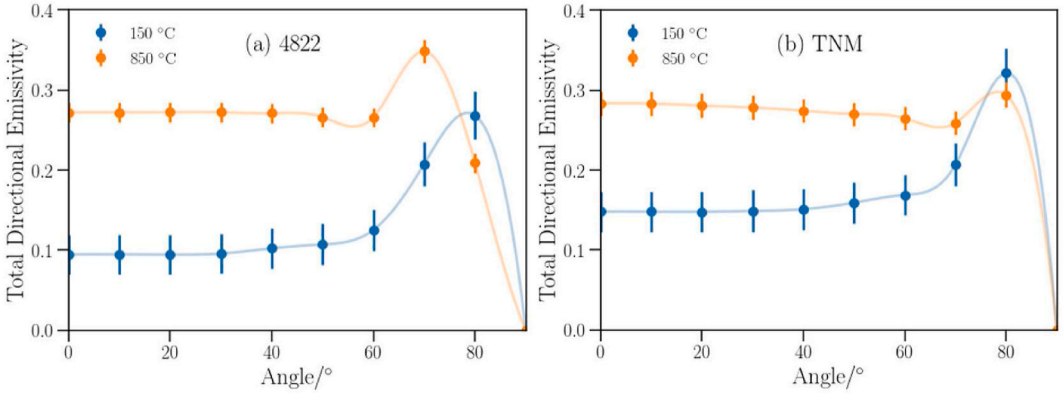

Fig. 5. Evolution of the emissivity with inclination angle detection at the lowest (150 °C) and highest temperature (850 °C) for (a) 4822 alloy and (b) TNM alloy. Error bars correspond to expanded uncertainties (k = 2).

Furthermore, beneath the oxides particles observed in the top views shown in Fig. 7 a-b, additional oxide particles may also be present, which would contribute to the thickness determined by XPS depth profiling, but cannot be considered in the estimation done from the SEM images.

Apart from oxidation, if we compare the microstructure of the TNM cross-section with the starting one shown in Fig. 1, a change of the microstructure can be observed in the BSE images of the corresponding cross-section (Fig. 7d). This evolution of the microstructure is notable in the β_o phase, the brighter phase in the corresponding BSE image, where needle-shaped precipitates formed, giving rise to a basket-weave structure that has been previously reported [9,12]. According to Sallot et al. [12], these precipitates arise due to the decomposition of the β_o phase into γ phase and, in particular, into α_2 phase. In the present work, the oxidation has taken place under a vacuum of $4{\cdot}10^{-4}$ mbar and no variation has been observed in the γ or α_2 grains, as occurred in the oxidation works carried out in air at high temperatures [9,12,13]. An observable evolution of the microstructure in the β_o phase and not in the α_2 phase occurs because there is a greater solubility of O in the α_2 phase, as stated in [10], which produces a stabilization of the α_2 phase compared to the β_o phase by O. Due to this α-stabilizing effect, there is no reason for the already present α_2 phase to transform while the O content in the material remains below its solubility limit. The observed microstructure change in TNM alloy only occurs in the subsurface down to 1.75 μm and not in the bulk where the microstructure remains stable. In the case of the 4822 alloy, such microstructural evolution of the β_o phase

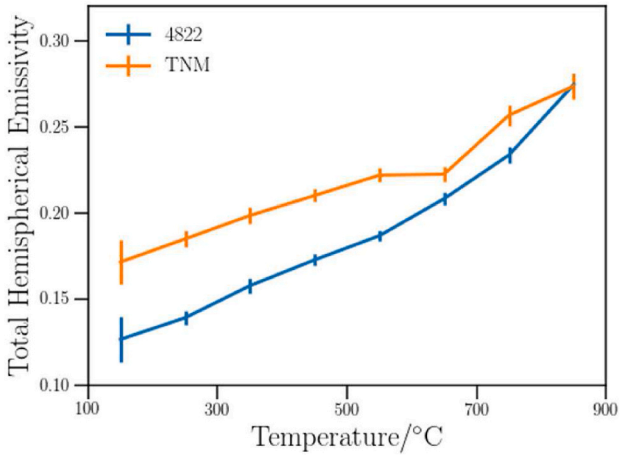

Fig. 6. Evolution of hemispherical emissivity with temperature for the 4822 (blue) and TNM (orange) alloys. Error bars correspond to expanded uncertainties ($k = 2$).

has not been observed. This is in agreement with the work carried out by Sallot et al. [12] where a pronounced change of the β_o phase was observed for the TNM alloy, but not for the 4822 alloy. In order to analyze this different behavior, it is interesting to mention that three thermally activated relaxation processes related with short-range diffusion processes have been identified and reported for the TiAl alloys via internal friction measurements between 690 °C and 800 °C [30,31]: a reorientation of the elastic dipole composed of two atoms of aluminum and one vacancy of titanium (Al–V_{Ti}–Al) provided by Ti diffusion in α_2 phase, an Al–V_{Ti} exchange by Al diffusion in γ phase [31] and Mo–Mo elastic dipole reorientation provided by Mo diffusion through V_{Ti} and V_{Al} vacancies occurring within the β_o phase [30]. Therefore, it is evident that Mo plays a fundamental role in the diffusion processes that occur in the β_o phase. Hence, it is reasonable to interpret the evolution of the microstructure of the β_o phase in the sub-surface region in terms of the diffusion of Mo and O. In the case of the 4822 alloy, the presence of β_o phase is significantly lower than in TNM alloy (Fig. 1) and there is no Mo in the nominal composition, what consequently leads to no decomposition of that phase. An additional reason for the absence of any decomposition of the β_o phase in the 4822 alloy might be attributed to the fact that there are no β_o "channels" from the surface into the material present like in the TNM alloy, due to the low overall β_o content in the 4822 alloy. As the O diffusion can be expected to be lower in the other phases, there may not be enough O inward diffusion in order to transform even the β_o grains, which are situated only a few microns below the surface.

It is important to remark that the values of the emissivity and its evolution also depend on the microstructure, rather than simply on the surface roughness as is often assumed. Indeed, a previous study performed on alloys with the HAIRL emissometer, had demonstrated that the presence of secondary phases and other diffusion processes in alloys have measurable consequences on the emissivity [15]. Therefore, as both alloys studied in the present work had the same initial surface conditions (same surface polishing), it is reasonable to consider that the differences in emissivity measurements (Figs. 4–6) at low temperature between both alloys correspond mainly to their different β_o phase amount. Hence, as the TNM alloy presents greater emissivity values at low temperatures, for which no microstructural evolution is expected, it may be concluded that the β_o phase provides a higher emissivity value than its homologous phases. By comparison, the variation in emissivity with temperature is more pronounced for the 4822 alloy primarily due to an oxidation process that results in slightly larger oxide particles than in the TNM alloy. In addition, in the case of TNM, apart from the slight oxidation that increases the emissivity, the evolution of the microstructure of the β_o phase at high temperatures must be taken into account, which gives rise to $\beta_o \rightarrow \alpha_2 + \gamma$ transformation and reduces the proportion of β_o phase and, hence, the emissivity. These two processes,

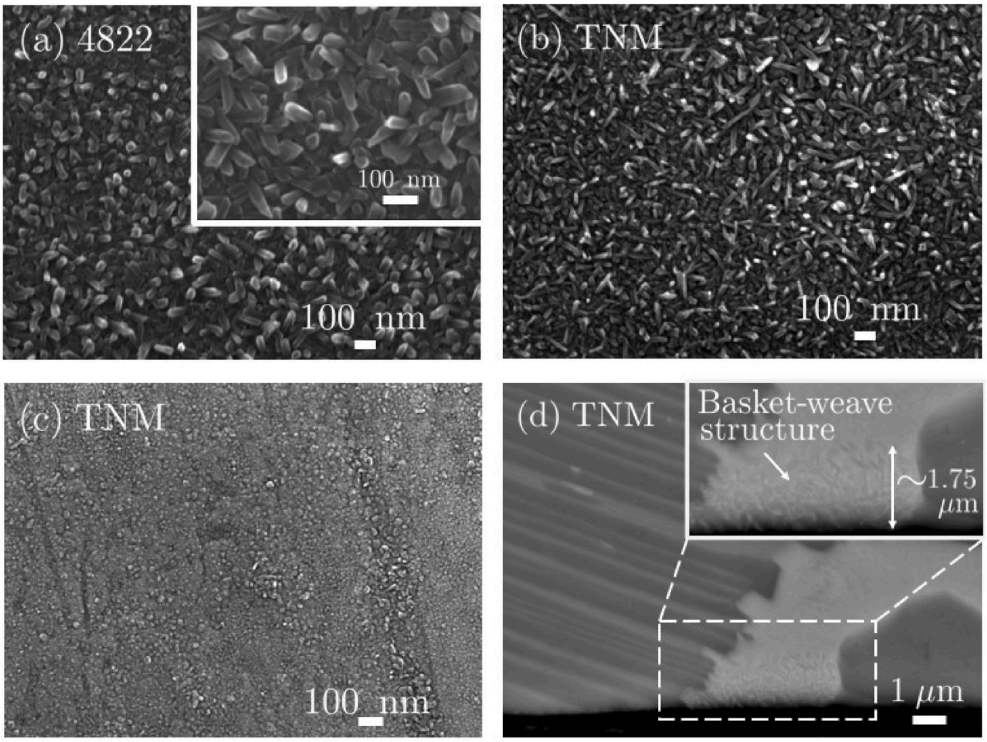

Fig. 7. Secondary electron (SE) images of the oxide particles in the 4822 alloy at different magnifications (a), and in TNM alloy in two different regions (b) and (c) after directional emissivity measurements under vacuum ($4 \cdot 10^{-4}$ mbar) at different temperatures up to 850 °C; (d) cross-section BSE images of the TNM surface after the emissivity measurements.

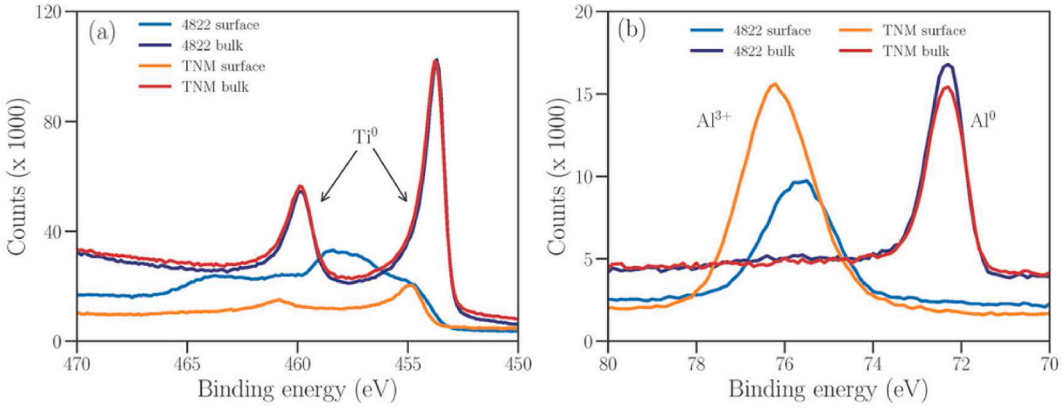

Fig. 8. XPS characterization of the 4822 and TNM samples after emissivity measurements under vacuum up to 850 °C. XPS spectra of the Ti (a) and Al (b) in the initial and final states, respectively, after sputtering for both alloys.

the oxidation and the destabilization of the β_o phase, have an opposite effect on the emissivity, which could explain lower evolution of the emissivity with temperature in the case of the TNM alloy.

3.3. Emissivity measurements during oxidation

After measuring the directional spectral emissivity, samples from both alloys were oxidized in laboratory air at 750 and 850 °C for 120 h and the near-normal emissivity was continuously measured to observe its evolution as they oxidize. Fig. 9 shows the spectral emissivity measurements at 10° (near-normal emissivity). Absorption peaks from water (around 2.7 and 5–8 μm) and CO_2 (around 4.2 μm) are present due to open-air measurements. The oxide layer growth leads to several changes in the emissivity spectra. At the initial stages, an uptick in the emissivity at shorter wavelengths is normally seen. After that, as it can clearly be seen in the 850 °C measurements, maxima and minima start to appear. When the oxide layer is semi-transparent, light interference occurs, creating maxima and minima in the emission spectrum [16]. As the layer thickness increases, these extremes shift towards longer wavelengths and higher order ones start to appear. At the later stages of the oxidation process, the oxide layer starts to become opaque for certain wavelengths up to the point where the observed emissivity approaches that of the pure oxide and the substrate does not longer contribute to the optical properties of the sample in the studied spectral range. The data shown in Fig. 9 indicate that the 4822 alloy oxidizes more quickly than the TNM alloy, especially at 750 °C. In both samples, interferential maxima and minima appear at higher temperatures, whereas at lower temperatures they can only be clearly seen in the 4822 alloy. This fact indicates that the TNM alloy, during the heat treatment in air at 750 °C, undergoes a less pronounced oxidation and that the thin oxide layer generated in

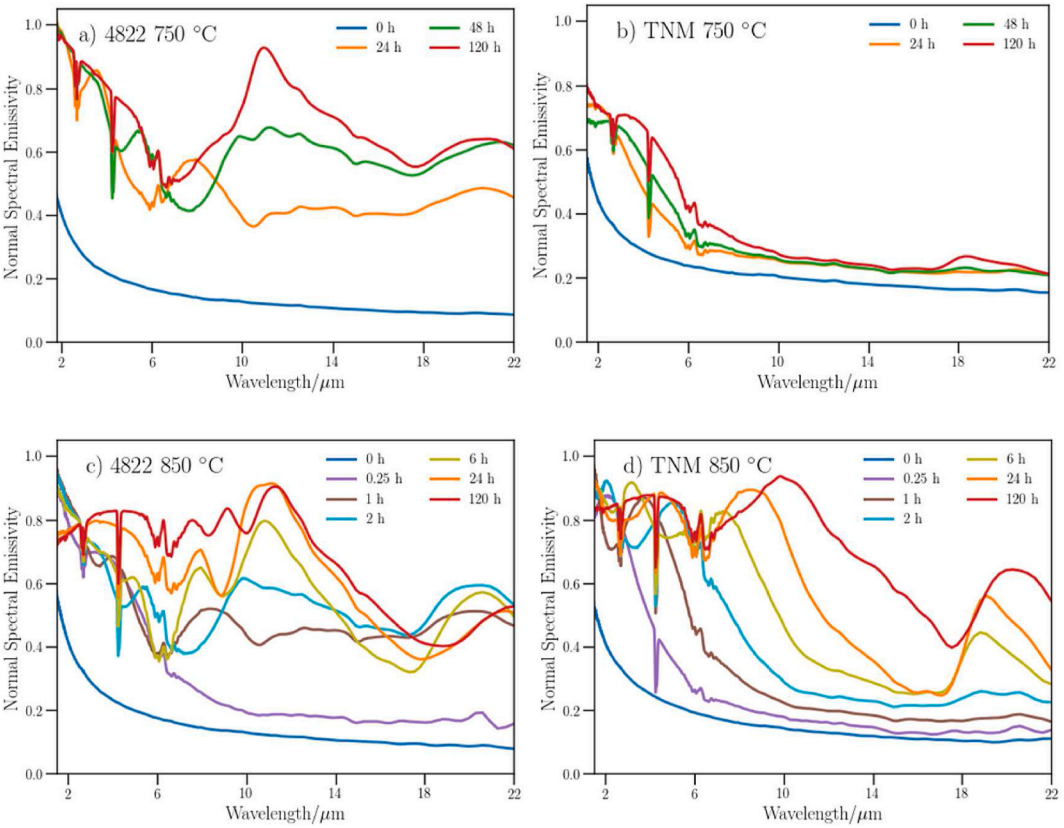

Fig. 9. Near-normal emissivity measurements of both the 4822 and TNM alloy at 750 and 850 °C during an oxidation process of 5 days (120 h).

these early stages does not produce interferential maxima and minima. Thus, according to the emissivity measurements, the TNM exhibit higher oxidation resistance especially at 750 °C. Besides, for both alloys the appearance of a non-interferential maximum around 11 μm at high temperatures can be related to the so-called Christiansen point of the rutile TiO_2 (with Christiansen wavelengths around 11.1 and 11.6 μm for parallel and perpendicular polarizations respectively) and/or alumina (with a Christiansen wavelength around 10.2 μm) [32,33].

The surface of both alloys after the thermal treatments in air for 120 h has been analyzed for both temperatures, as shown in Fig. 10. The top view of the 4822 alloy after the oxidation at 750 °C (Fig. 10a) and EDX analysis reveal two kinds of oxide particles: oxide particles with flat facets and a higher Ti content that correspond to TiO_2 rutile oxide, and globular-shaped Al_2O_3 alumina particles with higher Al content. In the TNM sample oxidized at the same temperature (Fig. 10b), the pattern is not as clear since the oxide particles are significantly smaller and the morphology is not as pronounced. In the case of the top view of the 4822 alloy oxidized at 850 °C (Fig. 10c), the rutile oxides cover practically the entire surface, whereas in the TNM alloy (Fig. 10d), two types of oxides are observed, rutile in the outermost positions and alumina in innermost ones. For both temperatures, the oxide particles are smaller for the TNM alloy, which is consistent with the lower degree of oxidation suggested by the emissivity measurements. The cross-sections of the surface after oxidation confirm that the oxide scales formed at 750 °C and at 850 °C are thinner for the TNM alloy (Fig. 10f and h) when compared to the 4822 alloy (Fig. 10e and g). At 750 °C, the oxide scale thickness of the TNM alloy is ~0.8 μm, whereas the one of the 4822 alloy is ~5 μm. At 850 °C the oxide scale thicknesses in the two alloys are ~7 μm and ~10 μm, respectively. These results confirm the better oxidation resistance of TNM alloys. The BSE images of the cross-sections, Fig. 10 e-h, illustrate that the oxide scales are composed of four different layers for both alloys at both temperatures, which is in good agreement with previous work in literature [9,10,13]. Complementarily, EDX element map analysis for the 4822 and TNM alloy after oxidation at 850 °C are presented in Fig. 11. This analysis suggests that the outermost layer is a Ti-rich layer composed of rutile oxide, the second one is an alumina layer, the third one is a mixture of alumina and rutile and the last one is a Nb-rich nitride layer.

Furthermore, EDX analysis reveals that the concentration of the heaviest atoms, Nb in the case of 4822 and Nb and Mo in the case of TNM, is almost negligible in the first oxide layer and low in the second layer. In this second layer, these heavy atoms are located at the bottom, close to the third layer. This fact, together with the high porosity of these two layers and the distinct morphology of the rutile particles in the first layer and the alumina particles in the second layer (Fig. 10 a-d), suggests that the growth of these two layers occurred outwards. On the contrary, the third and the fourth layer, with a lower concentration of O and a greater presence of heavy elements, grew inwards. The third layer is generally considered to be a mixture of alumina and rutile oxides [9,10,13], which is consistent with the electron microscopy images and the compositional analysis performed. However, it is important to note that the amount of Al is significantly lower than that of Ti in this region, which suggests that rutile is the main oxide in this mixture. The maxima and minima in the emissivity measurements during the oxidation at the higher temperature arise from the interference of the emitted radiation coming from two parallel interfaces. However, the first and second outermost layers generated by outgrowth are very rough, as shown in Fig. 10 a-d, and should not be capable of generating interference patterns. The third layer, which grows inwards, is the one with the most suitable morphology and thickness for the production of interference maxima and minima, since the fourth layer is too thin to be able to generate interferences in the wavelength range studied. Thus, it is consider that this mixed TiO_2/Al_2O_3 layer governs the interferential part of the alloys' emissivity spectra. This contribution in combination with the background, which is produced by all oxide layers, will determine the radiative heat transfer of the alloys in oxidizing service conditions. Further studies are required to separate the individual contributions of each layer. Regarding the surface composition, it is worth mentioning that nitridation plays an important role in the oxidation behavior of γ-TiAl alloys [34,35], in the current work the detected amount of N is very low, almost negligible, compared with the other elements. These N atoms are located in the outermost Ti rich oxide layer and in the innermost Nb rich nitride one and it is unlikely that they can have an influence on the emissivity.

In addition, the cross-section of the TNM alloy after oxidation at 750 °C (Fig. 10f), shows microstructural evolution of the sub-surface region due to the decomposition of the β_o phase into α_2 phase that forms the basket weave structure. In the former β_o phase of the TNM alloy oxidized at 850 °C (Fig. 10h), a coarsening of needle-shaped α_2 phase with respect to the sample oxidized at 750 °C is detected. These results are in good agreement with previous works as reported in Refs. [9,10].

XRD patterns were also acquired to investigate the structure of the oxide layers. These results confirm the presence of rutile and alumina for the samples oxidized at 850 °C during 120 h, as shown in Fig. 12. In the case of the 4822 sample (Fig. 12a), the relative intensities of the peaks associated with the γ-TiAl phase are smaller than in the case of the TNM sample (Fig. 12b), as could have been expected since the thickness of the

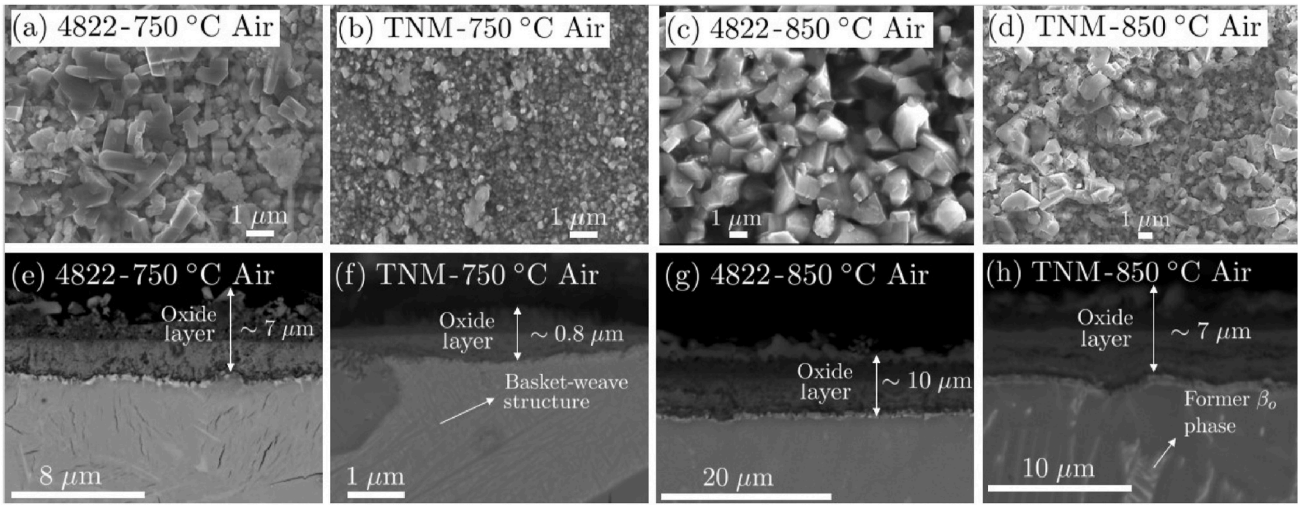

Fig. 10. SEM images taken in SE mode of the top views of the surface of the 4822 and TNM alloy after oxidation in air for 120 h at 750 °C (a and b) and at 850 °C (c and d), and cross-sectional SEM/BSE images to the oxide layer of the samples oxidized at 750 °C (e and f) and 850 °C (g and h).

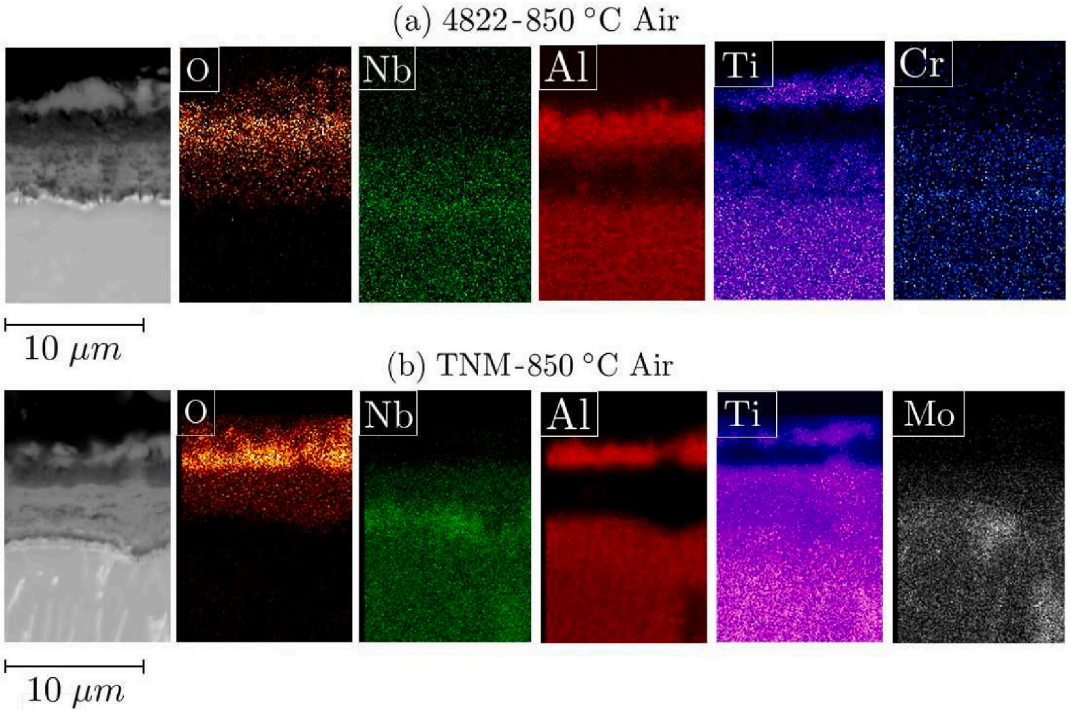

Fig. 11. Cross-sectional SEM images taken in BSE mode of the oxide layers and their corresponding EDX element map for the 4822 (a) and TNM (b) alloys after oxidation in air during 120 h at 850 °C.

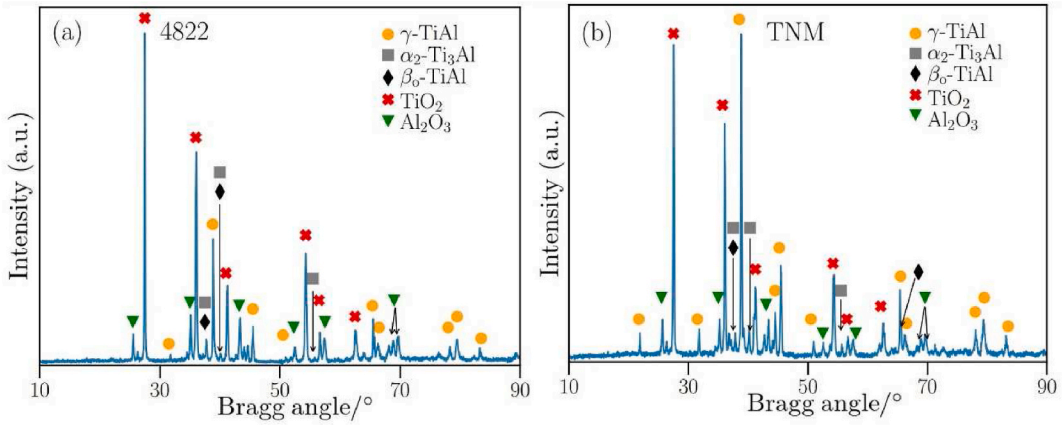

Fig. 12. X-ray patterns for 4822 (a) and TNM (b) samples oxidized in air at 850 °C for 120 h (see text).

oxide layer is greater for the 4822 alloy. The intensity corresponding to the different peaks of the rutile is significantly larger than the intensity associated with the alumina ones, indicating that there is a greater amount of rutile, which was also observed in the cross-section of the samples (Fig. 10g and h).

4. Conclusions

Both directional and hemispherical emissivity data have been obtained under vacuum for the 4822 and TNM alloy in the 150–850 °C temperature range. The differences in the emissivity values between both alloys at the lowest temperatures, for which the observed microstructures are expected to be thermally stable, suggests that the β_o phase, present in TNM and almost negligible in the 4822 alloy, exhibit higher emissivity values. There is a smaller change of the normal and hemispherical emissivity with temperature in the TNM alloy when compared to the 4822 alloy.

At 850 °C the total hemispherical emissivity in vacuum are nearly identical with 0.274 ± 0.006 for the 4822 alloy and 0.273 ± 0.007 for the TNM alloy. Thin oxide layers of a few hundreds of nanometers are formed during the emissivity measurement up to 850 °C on both alloys. In the case of the TNM alloy, decomposition of the β_o phase into the α_2 phase in the subsurface region has been detected. This evolution of the β_o phase and the lower final oxidation are consistent with the less pronounced change of the emissivity with temperature of the TNM alloy when compared to the 4822 alloy.

Isothermal oxidation processes in air at 750 °C and 850 °C of both alloys have been characterized via normal emissivity measurements. The maximum emissivity for both alloys is very close to the Christiansen points of rutile and alumina. Besides, the obtained oxidation morphology and composition agrees with four distinguishable layers: an outer layer of TiO_2 contiguous with a layer of Al_2O_3, followed by a mixed layer composed of TiO_2 and Al_2O_3 and finally a thin layer of Nb-rich nitride. The present morphological and compositional study of the

different oxide layers suggests that the third layer, which consists of a mixture of rutile and alumina, is responsible for the observed interferential minima and maxima in the normal emissivity signal and plays a fundamental role in the values of emissivity and, therefore, on the heat transfer at high temperatures.

Declaration of competing interest

The authors declare that they have no known competing financial interests or personal relationships that could have appeared to influence the work reported in this paper.

Acknowledgments

This work was supported by the Education Department of Basque Government via PIBA-PUE2021_1_0022 and IT-1714-22 projects as well as a predoctoral grant (M. Sainz-Menchón: PRE-2022-1-0086). The authors thank for technical and human support provided by SGIker of UPV/EHU and European funding (ERDF and ESF) as well as R. Wartbichler for sample preparation and helpful discussions.

References

[1] Reed RC. The superalloys: fund. And applications. Cambridge University Press; 2006.
[2] Pollock TM, Tin S. Nickel-based superalloys for advanced turbine engines: chemistry, microstructure and properties. J Propul Power 2006;22:361–74.
[3] Bewlay B, Weimer M, Kelly T, Suzuki A, Subramanian PR. In: Heilmaier M, Baker I, Kumar S, Yoshimi K, editors. Mater. Res. Soc. Symp. Proc. 1516. Cambridge University Press; 2013. p. 49–58.
[4] Boyer RR, Williams JC, Zhou L, Chang H, Lu Y, Xu D, editors. Proc. Of the 12th world conf. On titanium 2011. Beijing: Science Press; 2012. p. 10–9.
[5] Clemens H, Mayer S. Design, processing, microstructure, properties, and applications of advanced intermetallic TiAl alloysDesign, processing, microstructure, properties, and applications of advanced intermetallic TiAl alloys Adv. Eng Mater 2013;15:191–215.
[6] Hauptmann D. Report MTU Aero Engines 2013;1:24.
[7] Kim Y, Kim S. Advances in gammalloy materials-processes-application technology: successes, dilemmas, and future. JOM 2018;70:553–60.
[8] Schwaighofer E, Clemens H, Mauer S, Lindemann J, Klose J, Smarsly W, et al. Microstructural design and mechanical properties of a cast and heat-treated intermetallic multi-phase γ-TiAl based alloy. Intermetallics 2014;44:128–40.
[9] Mengis L, Ulrich AS, Watermeyer P, Liebscher CH, Galetz MC. Oxidation behavior and related microstructural changes of two β_o -phase containing TiAl alloys between 600°C and 900°C. Corrosion Sci 2021;178:109085.
[10] Galetz MC, Ulrich AS, Oskay C, Fähsing D, Laska N, Schulz U, et al. Oxidation-induced microstructural changes of the TiAl TNM-B1 alloy after exposure at 900 °C in air. Intermetallics 2020;123:106830.
[11] Pflumm R, Donchev A, Mayer S, Clemens H, Schütze M. High-temperature oxidation behavior of multi-phase Mo-containing γ-TiAl-based alloys. Intermetallics 2014;53:45–55.
[12] Sallot P, Monchoux JP, Joulié S, Couret A, Thomas M. Impact of β-phase in TiAl alloys on mechanical properties after high temperature air exposure. Intermetallics 2020;119:106729.
[13] Donchev A, Mengis L, Couret A, Mayer S, Clemens H, Galetz M. Effects of tungsten alloying and fluorination on the oxidation behavior of intermetallic titanium aluminides for aerospace applications. Intermetallics 2021;139:107270.
[14] Siegel R, Howell J. Thermal radiation heat transfer. 4th ed. Washington: Taylor & Francis; 2002.
[15] Echániz T, de Arrieta IG, Fuente R, Urcelay-Olabarria I, Igartua JM, de la Pinta N, et al. Thermal radiative properties of electron-beam-melted and mechanically alloyed V-4Cr-4Ti based alloys between 200 and 750 °C. J Nucl Mater 2019;513:86–93.
[16] de Arrieta IG, González L, Risueño E, Echániz T, Tello MJ. Isothermal oxidation kinetics of nitrided Ti-6Al-4V studied by infrared emissivity. Corrosion Sci 2020;173:108723.
[17] Balat-Pichelin M, Sans JL, Bèche E, Flaud V, Annaloro J. Emissivity at high temperature of Ni-based superalloys for the design of solar receivers for future tower power plants. Mater Char 2017;127:379–90.
[18] Greene GA, Finfrock CC, Irvine Jr TF. Total hemispherical emissivity of oxidized Inconel 718 in the temperature range 300-1000 °C. Exp Therm Fluid Sci 2000;22:145–53.
[19] Froes F, Boyer R. Additive manufacturing for the aerospace industry. Elsevier; 2019.
[20] Dutta B, Froes FH. The Additive Manufacturing (AM) of titanium alloys. Met Powder Rep 2017;72 2:96–106.
[21] Moges T, Ameta G, Witherell P. A review of model inaccuracy and parameter uncertainty in laser powder bed fusion models and simulations. J Manuf Sci E-T ASME 2019;141:040801.
[22] Güther V, Allen M, Klose J, Clemens H. Metallurgical processing of titanium aluminides on industrial scale. Intermetallics 2018;103:12–22.
[23] González de Arrieta I, Echániz T, Fuente R, Campillo-Robles JM, Igartua JM, López GA. Updated measurement method and uncertainty budget for direct emissivity measurements at the University of the Basque Country. Metrologia 2020;57:045002.
[24] Joint Committee for Guides in Metrology. Evaluation of measurement data - supplement 1 to the "guide to the expression of uncertainty in measurement"- propagation of distributions using a Monte Carlo method, technical report. JCGM 2008;101(2008).
[25] del Campo L, Pérez-Sáez RB, González-Fernández L, Esquisabel X, Fernández I, González-Martín P, et al. Emissivity measurements on aeronautical alloys. J Alloys Compd 2010;489:482–7.
[26] Kong B, Li T, Eri Q. Normal spectral emissivity measurement on five aeronautical alloys. J Alloys Compd 2017;703:125–38.
[27] Xu Y, Zhang K, Yu K, Liu Y, Liu Y. Temperature-dependent emissivity models of aeronautical alloy DD6 and modified function for emissivity computation with different roughness. Int J Thermophys 2021;42:7.
[28] González de Arrieta I, Echániz T, Fuente R, Rubin E, Chen R, Igartua JM, et al. Infrared emissivity of copper- alloyed spinel coatings for concentrated solar power systems. Sol Energy Mater Sol Cell 2019;200:109961.
[29] González-Fernández L, Risueño E, Pérez-Sáez RB, Tello MJ. Infrared normal spectral emissivity of Ti–6Al–4V alloy in the 500–1150K temperature range. J Alloys Compd 2012;541:144–9.
[30] Usategui L, No ML, Mayer S, Clemens H, San Juan J. Internal friction and atomic relaxation processes in an intermetallic Mo-rich Ti-44Al-7Mo ($\gamma+\beta_o$) model alloy. Mater Sci Eng, A 2017;700:495–502.
[31] Usategui L, Klein T, No ML, Mayer S, Clemens H, San Juan J. High-temperature phenomena in an advanced intermetallic nano-lamellar γ-TiAl-based alloy. Part I: internal friction and atomic relaxation processes. Acta Mater 2020;200:442–54.
[32] González de Arrieta I, González-Fernández L, Echániz T, del Campo L, De Sousa Meneses D, López GA. Small-polaron-induced infrared opacification in rutile TiO_2. J Appl Phys 2021;130:075105.
[33] Rousseau B, de Brun JF, De Sousa Meneses D, Echegut P. Temperature measurement: christiansen wavelength and balckbody reference. Int J Thermophys 2005;26:1277–86.
[34] Mathabathe MN, Govender G, Siyasiya GW, Mostert RJ, Bolokang AS. Surface characterization of the cyclically oxidized γ-Ti-48Al-2Nb-0.7 Cr alloy after nitridation. Mater Char 2019;154:94–102.
[35] Mathabathe MN, Bolokang AS, Govender G, Mostert RJ, Siyasiya CW. The vacuum melted ɣ-TiAl (Nb, Cr, Si)-doped alloys and their cyclic oxidation properties. Vacuum 2018;154:82–9.